Atmos. Chem. Phys. Discuss., 10, 28963–29005, 2010
www.atmos-chem-phys-discuss.net/10/28963/2010/
doi:10.5194/acpd-10-28963-2010

Atmospheric Chemistry and Physics Discussions

A new estimation of the recent tropospheric molecular hydrogen budget using atmospheric observations and variational inversion

C. Yver[1], I. Pison[1,2], A. Fortems-Cheiney[1], M. Schmidt[1], P. Bousquet[1,2], M. Ramonet[1], A. Jordan[3], A. Søvde[4], A. Engel[5], R. Fisher[6], D. Lowry[6], E. Nisbet[6], I. Levin[7], S. Hammer[7], J. Necki[8], J. Bartyzel[8], S. Reimann[9], M. K. Vollmer[9], M. Steinbacher[9], T. Aalto[10], M. Maione[11], I. Arduini[11], S. O'Doherty[12], A. Grant[12], W. Sturges[13], C. R. Lunder[14], V. Privalov[15], and N. Paramonova[15]

[1]Laboratoire des Sciences du Climat et de l'Environnement (LSCE), UMR 8212, Gif sur Yvette, France
[2]Université de Versailles Saint Quentin en Yvelines (UVSQ), Versailles, France
[3]Max Planck Institut für Biogeochemistry, 07701 Jena, Germany
[4]Department of Geosciences, University of Oslo, P.O. Box 1022, Blindern, 0315 Oslo, Norway

[5] Institut für Meteorologie und Geophysik, Johann Wolfgang Goethe-Universität Frankfurt, Frankfurt, Germany
[6] Department of Geology, Royal Holloway, University of London, Egham, UK
[7] Institut für Umweltphysik, University of Heidelberg, Heidelberg, Germany
[8] Faculty of Physics and Applied Computer Science, AGH-University of Science and Technology, 30-059 Krakow, Al. Mickiewicza 30, Poland
[9] Empa, Swiss Federal Institute for Materials Science and Technology, Laboratory for Air Pollution/Environmental Technology, Ueberlandstrasse 129, 8600 Duebendorf, Switzerland
[10] Finnish Meteorological Institute, Climate Change Research, P.O. Box 503, 00101 Helsinki, Finland
[11] Università degli Studi di Urbino, Istituto di Scienze Chimiche, Piazza Rinascimento 6, 61029 Urbino, Italy
[12] School of Chemistry, University of Bristol, UK
[13] School of Environmental Sciences, University of East Anglia, Norwich, UK
[14] Norwegian Institute for Air Research, P.O. Box 100, 2027 Kjeller, Norway
[15] Voeikov Main Geophysical Observatory, St. Petersburg, Russia

Received: 18 October 2010 – Accepted: 18 November 2010 – Published: 25 November 2010

Correspondence to: C. Yver (camille.yver@lsce.ipsl.fr)

Published by Copernicus Publications on behalf of the European Geosciences Union.

Abstract

This paper presents an analysis of the recent tropospheric molecular hydrogen (H_2) budget with a particular focus on soil uptake and surface emissions. A variational inversion scheme is combined with observations from the RAMCES and EUROHYDROS atmospheric networks, which include continuous measurements performed between mid-2006 and mid-2009. Net H_2 surface flux, soil uptake distinct from surface emissions and finally, soil uptake, biomass burning, anthropogenic emissions and N_2 fixation-related emissions separately were inverted in several scenarios. The various inversions generate an estimate for each term of the H_2 budget. The net H_2 flux per region (High Northern Hemisphere, Tropics and High Southern Hemisphere) varies between −8 and 8 Tg yr^{-1}. The best inversion in terms of fit to the observations combines updated prior surface emissions and a soil deposition velocity map that is based on soil uptake measurements. Our estimate of global H_2 soil uptake is -59 ± 4.0 Tg yr^{-1}. Forty per cent of this uptake is located in the High Northern Hemisphere and 55% is located in the Tropics. In terms of surface emissions, seasonality is mainly driven by biomass burning emissions. The inferred European anthropogenic emissions are consistent with independent H_2 emissions estimated using a H_2/CO mass ratio of 0.034 and CO emissions considering their respective uncertainties. To constrain a more robust partition of H_2 sources and sinks would need additional constraints, such as isotopic measurements.

1 Introduction

With a mixing ratio of about 530 ppb (part-per-billion, 10^{-9}), tropospheric H_2 is the second most abundant reduced trace gas in the troposphere after methane (CH_4). In contrast to CH_4 and other trace gases sharing anthropogenic sources, the observed H_2 mixing ratios are lower in the Northern Hemisphere when compared to the Southern Hemisphere due to the distribution of the sources and sinks of H_2 (Novelli et al., 1999).

ACPD
10, 28963–29005, 2010

The mean strength of each term of the H_2 budget is given hereafter as referred to in the literature (Novelli et al., 1999; Hauglustaine and Ehhalt, 2002; Sanderson et al., 2003; Xiao et al., 2007; Price et al., 2007; Ehhalt, 2009). The main sources of H_2 are photochemical production by the transformation of formaldehyde (HCHO) in the atmosphere and incomplete combustion processes. Photolysis of HCHO, a product in the oxidation chain of methane and other volatile organic compounds (VOCs) accounts for 31 to 77 $Tg\,yr^{-1}$ and represents half of the total H_2 source. Fossil fuel and biomass burning emissions, two incomplete combustion sources, account for similar shares of the global H_2 budget (10–23 $Tg\,yr^{-1}$, or 20% each). Minor H_2 emissions originate from nitrogen fixation in the continental and marine biosphere and complete the sources (6–11 $Tg\,yr^{-1}$). H_2 oxidation by free hydroxyl radicals (OH) and enzymatic H_2 destruction in soils must balance these sources because tropospheric H_2 does not show a significant long term trend (Grant et al., 2010b). H_2 oxidation through OH accounts for 8 to 25 $Tg\,yr^{-1}$, which is equivalent to 20% to 30% of the total H_2 sink. H_2 soil uptake, the major sink in the budget (65 to 105 $Tg\,yr^{-1}$ or 70% to 80% of the total sink), is responsible for the observed latitudinal surface gradient. It is, however, relatively poorly constrained due to uncertainties regarding its associated physical and chemical processes. Specifically, H_2 uptake is driven by enzymatic and microbial activities linked to H_2 diffusivity, which depend mostly on soil moisture and temperature (Conrad and Seiler, 1981, 1985; Yonemura et al., 1999, 2000a,b; Lallo et al., 2008, 2009; Schmitt et al., 2009).

Although global studies of H_2 mixing ratios using observations from sampling networks began in the 1990s, Schmidt (1978) had already presented meridional profiles of the Atlantic Ocean from ship cruise measurements. Subsequently, Khalil and Rasmussen (1990) announced an increase in H_2 mean mixing ratio based on weekly samplings between 1985 and 1989 at six locations from 71.5° N to 71.4° S. Novelli et al. (1999) presented the first estimation of the H_2 budget using observations from the NOAA Earth System Research Laboratory network (52 stations), which covers mainly the Northern Hemisphere but also to some extent the Southern Hemisphere

ACPD
10, 28963–29005, 2010

with oceanic samplings and Antarctic sites. This network has been running for H_2 since 1989 with regards to the first sites and was extended progressively to include all of the 52 sites in 1994. The CSIRO Global Flask Sampling Network (ten stations) began sampling in 1992 with a larger focus on the Southern Hemisphere (Langenfelds et al., 2002). Finally, within the AGAGE programme (Advanced Global Atmospheric Gases Experiment), H_2 has been measured continuously since 1993 at two stations worldwide (Prinn et al., 2000). A small increasing trend was extracted from the analysis of the observations provided by the NOAA network (Novelli et al., 1999) whereas the CSIRO observations exhibited a small decrease (Langenfelds et al., 2002). Since 2006, in the frame of the European project EUROHYDROS, a H_2 monitoring network, focusing mainly on Europe (13 continuous and 5 flask sampling sites) but also worldwide through 10 flask sampling sites outside Europe, was developed (Engel, 2009). The French Atmospheric Network for Greenhouse Gases Monitoring (RAMCES), part of the Laboratory for Climate and Environmental Sciences (LSCE) has provided observations from 10 sites (one of them sampling continuously) to the EUROHYDROS network and contributed with nine additional sites to this study. Parallel to the observations, forward modelling studies were used to provide the first constraints on the H_2 budget (Hauglustaine and Ehhalt, 2002; Price et al., 2007). Nevertheless, since the soil sink, the major loss term, is only known with large uncertainties, it is represented in models with more or less simplified assumptions which lead to a wide range of estimations for every term of the budget and especially for the soil sink, ranging from 40 to 90 $Tg\,yr^{-1}$ (Ehhalt, 2009).

Atmospheric observations combined with a chemistry-transport model and prior information on surface fluxes and sources and sinks within the atmosphere allow (in a Bayesian inversion framework) to retrieve the estimations of the H_2 sources and sinks and their uncertainties. Atmospheric inversions have already been developed to study H_2, but the studies remain sparse: Xiao et al. (2007) have used a 2-D latitude-vertical 12 box model for atmospheric chemistry in an inversion framework combined with AGAGE, NOAA and CSIRO measurements to estimate the magnitude and variability

ACPD
10, 28963–29005, 2010

of H_2 sources and sinks for four semi-hemispheres over the 1993–2004 period. More recently, Bousquet et al. (2010) have provided an analysis of global-to-regional details in the H_2 budget before 2005 based on large regions, using a synthesis inversion, a 3-D chemistry transport model and discrete observations from the flask networks of NOAA and CSIRO.

In this paper, we present the mixing ratio measurements of the RAMCES and EUROHYDROS sampling networks (13 continuous stations and 25 flasks sampling sites) for H_2 since January 2005. These time series provide information on seasonal cycles and H_2 distribution with latitude. As no NOAA data were available for this period, we have chosen to use only the data from the RAMCES and EUROHYDROS networks. The observations from mid-2006 to mid-2009 are assimilated in a variational inversion to estimate the global H_2 budget. Contrary to Bousquet et al. (2010), the observations are continuous as well as discrete, from a more recent period and they are centred on Europe. Six different scenarios have been elaborated to progressively constrain the terms of the H_2 budget. The results, with a detailed analysis of Europe (where 27 of the 38 sites are located), are presented below.

2 Observational network

2.1 RAMCES flask sampling network

RAMCES network's central laboratory is located at Gif-sur-Yvette (GIF) near Paris, France. During the period between 2006 and 2009, the RAMCES network analysed air from 19 sampling sites in the world (see Fig. 1). At eighteen sites, flasks were sampled weekly or biweekly. At all of the sites except Ivvittut (Greenland) site, flask sampling began before the H_2 analyser was installed in the central laboratory of Gif-sur-Yvette to monitor other greenhouse gases (CO_2, CH_4, N_2O, SF_6, CO). At Gif-sur-Yvette, air is sampled continuously. Table 2 lists the RAMCES flask network sites used in this study (highlighted with a asterisk for the sites additional to the EUROHYDROS network).

ACPD
10, 28963–29005, 2010

They are distributed across latitudes from 40° S to 82° N and, for most of them, they provide access to background air that is representative of zonal mean atmospheric composition. At the sites of Tver (Russia), Hegyhatsal (Hungary), Griffin (Scottland) and Orléans (France), monthly to weekly light aircraft flights have sampled the troposphere between 100 and 3000 m. These sites were part of the CARBOEUROPE programme that ended in December 2008. Trainou (France), Puy de Dôme (France), Pic du Midi (France) and Hanle (India) are situated inland but, except for Trainou, which regularly encounters polluted air masses, they are situated at high altitude and away from local anthropogenic influences. All of the other ground sites are coastal and they encounter air masses characterized by long marine back-trajectories.

2.2 EUROHYDROS network

In the EUROHYDROS project (September 2006 to September 2009), twenty laboratories from ten different countries participated. In this study, atmospheric H_2 measurements at 31 sites performed by 13 laboratories running over the period 2006 to 2009, are used in the variational inversion (see Table 1, Table 2 and Fig. 1). At 13 sites, ambient air is continuously sampled. For three stations (Alert (Canada), Mace Head (Ireland) and Bialystok (Poland)), simultaneous sampling by different laboratories is performed. Seven stations (Egham (UK), Gif-sur-Yvette (France), Heidelberg (Germany), Helsinki (Finland), Krakow (Poland), Tver and Voiekovo (Russia)) sample air in urban or suburban conditions. Continental sites such as Trainou (France) or Schauinsland (Germany) encounter alternatively clean and moderately polluted air masses. At Mace Head, Finokalia (Greece), Troodos (Cyprus) and Begur (Spain), the sampled air is under clean maritime and moderately polluted influences. The remaining stations mainly encounter clean background air. For six sites (Alert, Mace Head, Schauinsland, Cabo Verde, Amsterdam Island and Neumayer (Antarctica)), hydrogen isotopes in the sampled flasks are analysed by the University of Utrecht.

During the project, H_2 soil deposition velocities were measured at different sites and with different methods (Lallo et al., 2008, 2009; Schmitt et al., 2009; Hammer and Levin,

ACPD
10, 28963–29005, 2010

2009; Yver et al., 2009; Schillert, 2010). Theses flux estimations were interpolated into a soil uptake map as detailed in Sect. 3.3.

2.3 Sampling technique

In the frame of the EUROHYDROS project, all laboratories were requested to follow the recommendation for good measurement practice, a protocol developed at the beginning of the project (Engel, 2009). The calibration and non-linearity correction strategy, the type of standard gas cylinders, pressure regulators and instrumental set-up were specified there. In particular, all the samples were measured using standard cylinders calibrated against the MPI2009 scale, which has been elaborated for the EUROHYDROS project (Jordan, 2007; Jordan and Steinberg, 2010).

Within the RAMCES network, we followed this strategy as described in detail by Yver et al. (2009). Briefly, a commercial gas chromatograph coupled with a reduction gas detector (RGD) from Peak Laboratories, Inc., California, USA is used to measure H_2 via the reduction of mercuric oxide and the detection of mercury vapour by UV absorption. Sixteen inlet ports are set up on a 16-port Valco valve to connect flask samples to the inlet system. To avoid contamination and reduce the flushing volume of the sample when measuring the flasks, all sample inlet lines can be separately evacuated. Pairs of flasks are sampled at the sites as a rule, to check for sampling error or any malfunction in the sampling equipment. Each flask is then analysed twice to check the reproducibility of the measurements. Statistics on pair and double injection analyses give a reproducibility below 1% (≈3 ppb).

The analysis technique for atmospheric H_2 within the EUROHYDROS network is for most of the laboratories also based on the separation with gas chromatography and the detection with a RGD. The methods, following the recommendation for good measurement practice, are described for some of the laboratories in the following papers: Bonasoni et al. (1997) for UNIURB (see Table 1 for complete name), Hammer et al. (2009); Hammer and Levin (2009) for UHEI-IUP, Aalto et al. (2009) for FMI, Grant et al. (2010b) for UOB and Bond et al. (2010) for EMPA.

ACPD
10, 28963–29005, 2010

To ensure the compatibility of the data of the different laboratories, regular calibration against the common scale but also comparison of measurements done at the same site (Alert or Mace Head for example) and comparison exercises (Star Robin and Round Robin) were performed. From these last comparisons, the agreement between the 13 laboratories was better than 1.4% (Engel, 2009).

2.4 Observations used in the inversion

The observations from the 38 RAMCES and EUROHYDROS sites are plotted in Fig. 2. The Figure presents the sites by latitude, from the north to the south. For the continuous stations, the daily means are plotted and mixing ratios above 800 ppb, which correspond to strong local pollution events, are excluded. The mean mixing ratios range from ≈500 ppb at Alert to ≈550 ppb at Neumayer with a maximum in the Tropics (≈570 ppb at Pondichery (India)). We observe a seasonal cycle at all of the sites but with a greater amplitude and deeper minima in the High Northern Hemisphere (HNH, above 30° N). In this hemisphere, the seasonal maximum (up to 540 ppb) occurs in the spring (April, May) and the minimum of ≈430 ppb is observed in the autumn (September, October). In the Northern Tropics (between 30° N and 0° N), the seasonal cycle is shifted by about two months (maximum July and minimum in December), whereas in the High Southern Hemisphere (HSH,below 30° S), the seasonal maximum occurs in the austral summer (January, February) reaching up to 580 ppb and the minimum occurs in mid austral winter (August, September) equaling 550 ppb. The maximum amplitude is found in the HNH with about 110 ppb peak-to-through and the minimum is found in the HSH with 30 ppb peak-to-through. These patterns reflect the differences in the location and timing of H_2 sources and sinks. In the HSH and the Tropics, the seasonal variations are mostly explained by the timing of biomass burning emissions and photochemical production, which peak in the summer. The higher minima than in the HNH can be explained by the smaller influence of the soil uptake in the HSH due to the smaller soil surface area in the HSH than in the HNH. In the HNH, the minimum is reached in the autumn when the soil uptake is strongest and the oxidation sources are

ACPD
10, 28963–29005, 2010

weaker compared to summer. The maximum occurs in the spring when the soil uptake is the weakest.

In Fig. 3, the latitudinal gradient is based on the mean mixing ratio at every site, except for the urban sites such as Heidelberg (Germany), Krakow (Poland), Egham (London suburb, UK) and Tver (Moscow suburb, Russia), where the anthropogenic pollution enhances the background level of H_2. As already described, the lower mixing ratios are measured in the HNH. Mean mixing ratios show an increase with decreasing latitudes until 30° S and then show a slight decrease from 30° S to 70° S. From the north to the south, the mean gradient is ≈50 ppb and from the north to the Tropics, it is ≈60 ppb. According to our colour scheme, the latitudinal gradient is plotted in September/October/November in red and in March/April/May in blue. As expected, in the HNH, the mixing ratios are lower in the autumn than they are in the spring. The latitudinal gradient is also larger in the autumn with ≈70 ppb than it is in the spring (≈35 ppb).

All of these patterns highlight the importance of the soil uptake in the spatiotemporal variations of the H_2 mixing ratios and the need to estimate its strength and variations better.

3 The variational inversion system

3.1 General settings of PYVAR/LMDz-SACS

We use a framework which combines three components: the inversion system PYVAR developed by Chevallier et al. (2005), the transport model LMDzt (Hourdin and Talagrand, 2006) and a simplified chemistry module called SACS (Simplified Atmospheric Chemistry System) (Pison et al., 2009). LMDzt is the off-line version of the general circulation model (GCM) of the Laboratoire de Météorologie Dynamique (LMDz) (Sadourny and Laval, 1984; Hourdin and Armengaud, 1999). Briefly, LMDzt is used with nineteen sigma-pressure levels in the vertical (first level thickness of 150 m,

ACPD
10, 28963–29005, 2010

resolution in the boundary layer of 300 to 500 m and ≈2 km at the tropopause) and a horizontal resolution of 3.75° × 2.5° (longitude-latitude). The air mass fluxes used off-line are pre-calculated by LMDz online GCM nudged on ECMWF analysis for horizontal wind. SACS is a simplified methane oxidation chain. SACS keeps only the main species and the major reactions. The intermediate reactions are regarded as very fast compared to the principal reactions. In the atmosphere, the oxidation by OH is the main sink of CH_4. This reaction is the first in a chain of photochemical transformations which lead to formaldehyde which is also produced from the degradation of volatile organic compounds (VOCs) in the continental boundary layer. H_2 is at the end of the reaction chain along with CO as a product of the transformation of formaldehyde:

$$HCHO + h\nu \longrightarrow H_2 + CO \quad (1)$$

Although OH is the essential modulator of this reaction chain, this short-lived compound (≈1 s) is not easily measurable on a global scale. Its concentration is estimated only in an indirect way: using methyl chloroform (CH_3CCl_3 or MCF) which reacts only with OH and the sources of which are quantified with acceptable accuracy (Krol et al., 2003; Prinn et al., 2005; Bousquet et al., 2005). The adequacy of SACS with the full chemistry-transport model LMDz-INCA is evaluated in Pison et al. (2009). These authors show that the differences between the two chemistry models are significantly smaller than the variability of the concentration fields of the species of interest. To obtain the initial conditions for the simulations with SACS, the full chemistry-transport model LMDz-INCA is used to establish fields of OH and VOCs that are consistent with the initial state of the system (Hauglustaine et al., 2004). The deposition velocities for H_2, reaction constants and photolysis rates are also given to PYVAR by LMDz-INCA (Hauglustaine and Ehhalt, 2002). SACS can be used to estimate the sources and sinks of CH_4, CO, HCHO and H_2. In this work, we focus on only H_2 and the fluxes of CO and CH_4 are assumed to have been optimised and their errors are set to ±1%, whereas the errors on H_2 are set to ±100%.

ACPD
10, 28963–29005, 2010

PYVAR is a Bayesian inference scheme formulated in a variational framework. It consists in the minimisation of a cost function $J(x)$:

$$J(\boldsymbol{x}) = (\boldsymbol{x} - \boldsymbol{x}_b)^T \mathbf{B}^{-1} (\boldsymbol{x} - \boldsymbol{x}_b) + (\mathcal{H}(\boldsymbol{x}) - \boldsymbol{y})^T \mathbf{R}^{-1} (\mathcal{H}(\boldsymbol{x}) - \boldsymbol{y}) \quad (2)$$

where $\boldsymbol{x}$ is the state vector containing the variables that need to be estimated at each model grid cell, $\boldsymbol{x}_b$ contains the prior values of the variables and $\boldsymbol{y}$ the observations and $\mathcal{H}$ is the operator representing the chemistry-transport model and the retrieval of the equivalent of the observations. **B** and **R** are the covariance matrices of the error statistics of $\boldsymbol{x}_b$ and $\boldsymbol{y}$, respectively. The state vector contains the emission fluxes (here for H_2) and the average production of HCHO in each cell at eight-day frequency, the average OH concentrations as described by Bousquet et al. (2005) (four latitudinal bands) at the same frequency and the initial conditions for the concentrations (here of H_2). The system finds the optimal $\boldsymbol{x}_a$ which fits the observations and the prior values as weighted by the covariance matrices **R** and **B**. Physical considerations as detailed in Chevallier et al. (2005), are used to infer the errors (variances, spatial and temporal correlations) of the prior. In this study, the errors are set to ±100% of the maximal flux in the grid cell over the inversion period for H_2, 1% of the flux for MCF (in order to constrain OH), CO, CH_4 and HCHO fluxes. The error of ±10% for OH concentrations is consistent with the differences between estimates of the OH concentrations of several studies (Krol et al., 2003; Prinn et al., 2005; Bousquet et al., 2005). Finally, the error on the initial concentrations of HCHO, MCF and H_2 is set at ±10%. Temporal correlations are neglected as the state vector is aggregated on a 8-day basis. The spatial correlation are defined by an e-folding length of 500 km on land and 1000 km for the sea and no-correlation between the land and sea. This approach was shown to be as performant as an approach based on more physical properties (Carouge et al., 2010). The observation error matrix **R** is supposed to be diagonal and filled with the standard deviation of the measurements. A minimum uncertainty of ±5 ppb for H_2 and ±1.2 ppt for MCF is fixed to account for a minimal representativity error.

The H_2 prior emissions and monthly deposition velocity maps are detailed in Hauglustaine and Ehhalt (2002). No emission inventory exists for H_2 emissions.

ACPD
10, 28963–29005, 2010

Therefore, as CO and H_2 share the same sources (transportation, biomass burning, methane and VOCs oxidation), the H_2 emissions distribution is inferred from the CO emissions distribution (Olivier et al., 1996; Granier et al., 1996; Brasseur et al., 1998; Hao et al., 1996). Emissions are then scaled to fit the estimates given by the various studies presented in Hauglustaine and Ehhalt (2002). N_2 fixation-related emissions are scaled from CO emission maps for marine emissions and from NO_x emission maps for terrestrial emissions (Erickson and Taylor, 1992; Müller, 1992). Finally, the soil sink is estimated using the dry deposition velocity for CO, which is based on net primary production variations and a ratio between the deposition velocity of H_2 and CO of 1.5 (Hough, 1991; Brasseur et al., 1998). This leads to deposition velocities between zero and 0.1 cm s^{-1}.

3.2 New developments in PYVAR/LMDz-SACS

In the version presented by Pison et al. (2009), the net flux of H_2 is inverted at the model resolution without separating the sources from the sinks. Only the OH sink can be calculated separately as the result of the optimisation of the concentration of OH. At each time step, the H_2 soil uptake is calculated according to:

$$H_{2\text{deposited}} = v_{\text{dep}}[H_2] \quad (3)$$

with v_{dep} representing a constant value at each pixel and time step read from the prior monthly deposition velocity map and $[H_2]$ representing the mixing ratio.

In this work, we have modified the code to infer separately the soil uptake from the surface sources, by adding the soil uptake specifically as an unknown variable in the state vector. Thus, v_{dep} is optimised at each time step and grid cell. In a further attempt to optimise each term of the H_2 budget, the sources are also separately inverted. The emissions are split into three components: fossil fuel, biomass burning and N_2 fixation-related emissions. Prior fossil fuel and biomass burning emissions are inferred from the recent bottom-up CO emission inventory from Lamarque et al. (2008), by applying a mass flux ratio H_2/CO of 0.034 and 0.02, respectively (Hauglustaine and Ehhalt, 2002;

ACPD
10, 28963–29005, 2010

Yver et al., 2009). N_2 fixation-related emissions remain as they were in the previous version and represent about 25% of the total emissions.

3.3 Scenarios elaborated for the inversion

Six scenarios have been elaborated (see Table 3). In scenario S0, we invert the net flux of H_2 using the emission and soil sink maps from Hauglustaine and Ehhalt (2002) as described previously. The first-guess modelling leads to a strong offset with a simulated mean mixing ratio ≈115 ppb higher than that observed. This can be attributed to the underestimation of the soil sink (Hauglustaine and Ehhalt, 2002).

In scenario S1, we have therefore scaled the initial mean mixing ratios to the observed mean mixing ratios. Moreover, we have used updated prior surface emission fluxes from Lamarque et al. (2008) with H_2/CO mass ratio of 0.034 and 0.02 for anthropogenic and biomass burning emissions, respectively (Hauglustaine and Ehhalt, 2002; Yver et al., 2009) and optimised HCHO concentrations from Bousquet et al. (2010). The soil sink map has been scaled by a ratio of 1.28 to take into account the hypothesised underestimation.

In scenarios S2 to S4, the soil sink is separated from the emissions and for each scenario, a different prior soil deposition velocity map is used. The S2 deposition velocity map is the same as that of S1. A bottom-up soil uptake estimation calculated by the Lund-Postdam-Jena Dynamic Global Vegetation Model (LPJ) (Sitch et al., 2003) gives us the map for S3. This model combines process-based, large-scale representations of terrestrial vegetation dynamics (with feedbacks through canopy conductance between photosynthesis and transpiration) and land-atmosphere carbon and water exchanges in a modular framework. Ten plants functional types are taken into account and responses to fire and vegetation densities are updated annually whereas vegetation and soil water dynamics are modelled on a daily time interval.

For S4, the monthly map was produced for the EUROHYDROS project by the OSLO CTM forward model in combination with soil deposition velocities estimated within the EUROHYDROS project with bottom-up and top-down methods (map prepared by Amund Søvde using data compiled in Schillert, 2010).

ACPD
10, 28963–29005, 2010

Finally, in scenario S5, surface emissions are further separated into three components: fossil fuel, biomass burning and N_2 fixation-related emissions. Scenario S5 uses the prior deposition velocity map from S4.

3.4 Characteristics of the soil deposition velocity maps

As stated in the previous paragraph, we use three different soil deposition velocity maps as prior in the model. These maps are presented in Fig. 4. They present some common large scale features but differ for the magnitude and distribution of regional uptake. On a large scale, the highest values are found during summer. In winter, the maximum values are located in the Southern Hemisphere and in summer they are located in the Northern Hemisphere except for the S3 map where high deposition velocities are found in the Southern Hemisphere throughout the year. The first two maps (S0 and S3) are more detailed since they are based on vegetation maps. The last one (S4) was created using deposition velocity measurements. These measurements remain sparse and were thus extrapolated to latitudinal bands. The first map (S0) that supposedly underestimates the soil sink is nevertheless the one having the greatest velocities, up to 0.14 cm s^{-1}, whereas the S3 map only reaches 0.07 cm s^{-1} and the Oslo one (S4) only reaches 0.06 cm s^{-1}. However, if we plot the mean latitudinal deposition velocity versus the latitude (on the lower panel), different patterns appear. S0, S3 and S4 present a similar global pattern in winter, whereas the summer total of S3 is smaller than it is in the two other maps. The yearly total reaches 42, 36 and 46 cm s^{-1} for S0, S3 and S4 respectively.

S3 is characterised by the absence of large spatiotemporal variations and the smallest global total value. In this map, there is no hotspot but a lower deposition velocity above 30° N than below (except for the Sahara region with the desert and Australia).

S0 presents important spatiotemporal variations with marked hotspots. In the winter, these hotspots are observed in Brazil and southern Africa (United Republic of Tanzania, Republic of Mozambique, Zambia and Angola). In summer, hotspots are observed mostly in North America and in the north of Russia.

ACPD
10, 28963–29005, 2010

In S4 map, the latitudinal deposition velocity presents spatiotemporal variations as well, but contrary to S0, there are no hotspots. In winter, the larger values are found in South America and southern Africa too but more so at the southern latitudes (Argentina and South Africa). Since the soil uptake is extrapolated from latitudinal bands, there are also large values in southern Australia. In summer, the greater deposition velocities are observed above 30° N.

The three maps thereby present great differences in their distribution and we can expect to find important differences in the first-guess simulations.

4 Results and discussion

4.1 Evaluation of the first-guess and inverse simulations

We present, in Fig. 5, the simulated and observed mixing ratios for four sites: the northernmost site, Alert in Alaska, a mid-latitudinal site, Mace Head in Ireland, a northern tropical site, Pondichery in India and the southern hemispheric site, Amsterdam Island. Observations are plotted with black filled circles. Simulated mixing ratios are plotted in coloured diamonds with first-guess mixing ratios modelled with the prior emissions on the left panel and inverted mixing ratios on the right panel. As S1 and S2 as well as S4 and S5 use the same prior information, their first-guess mixing ratios are superimposed.

As previously mentioned, the first-guess mixing ratios using prior emissions from S0 are overestimated by about 115 ppb. For the other scenarios, the mixing ratios have been scaled and the prior fluxes have been updated so that the mean difference is lower than 40 ppb, except for S3, which presents a mean difference of 87 ppb due to a drift in time as the prior budget is not balanced. At Alert, the first-guess simulated seasonal cycle of S0 to S2 follows the observed cycle with a maximum in autumn and a minimum at the beginning of spring. For S3 through S5, the seasonal cycle is about two months late. At Mace Head, on the contrary, the first-guess simulated seasonal

ACPD
10, 28963–29005, 2010

cycle of S0 to S2 is about two months in advance, whereas S3, S4 and S5 follow the observed cycle. For the other sites, the weak seasonal cycle is well reproduced. The first-guess mixing ratios of S3, S4 and S5 present a qualitatively better agreement with the observed seasonal cycle. The seasonal amplitude is fairly reproduced by all of the first-guess simulations except for S3, for which the seasonal amplitude is weaker. For all of the sites, the first-guess mixing ratios of S3, S4 and S5 present a drift of 50, 30 and 30 ppb yr^{-1} respectively. This is due to the fact that the prior H_2 budget is not balanced since we use different soil deposition maps. We also see a slight decrease in S0 first-guess mixing ratios for Amsterdam Island which is not observed in the measurements.

After inversion, as expected, the simulated mixing ratios fit the observations better in terms of amplitude as well as seasonal cycle. The mean difference between observations and simulated mixing ratios is thus nearly zero. The mean coefficient of correlation between the observations and the simulations increases by ≈100%. The better correlation for the scenarios including the separate soil uptake optimisation is found for S4 with a mean difference around −1.5 ppb (+35 ppb for the first-guess), a standard deviation of 17 ppb (47 ppb for the first-guess) and a coefficient of correlation of 0.6 (0.4 for the first-guess). S5, where the sources are further separated presents very close results.

4.2 Inverted fluxes

For each process in the H_2 budget, the flux interannual variations remain small, below ±5 Tg yr^{-1}. All of the scenarios are consistent for the interannual variations in terms of pattern and amplitude (not shown). In Fig. 6, the mean seasonal cycle in 2006–2009 is plotted for all of the scenarios. For each process, we have studied three regions: the High Northern Hemisphere (HNH) above 30° N, the Tropics, between 30° N and 30° S and the High Southern Hemisphere (HSH) below 30° S. As explained before, H_2 photochemical production and OH loss are strongly constrained and therefore, the

ACPD
10, 28963–29005, 2010

inverted fluxes stay close to the prior fluxes. The difference of $\approx 5\,\mathrm{Tg\,yr^{-1}}$ between S0 and the others scenarios for the photochemical production is due to the change of the prior HCHO concentrations between the first scenario and the others. The priori soil uptake and the emissions are set with a error of 100% and are therefore more subject to changes. The soil uptake seasonal cycle presents large variations in the HNH. S0 and S1, where the soil uptake is not separately inverted, exhibit their maximum in June. For S2, with the separated inversion of the soil uptake, the maximum is shifted in July and for S3 and S4, the maximum is shifted in August. In comparison, the soil uptake measurements, obtained with bottom-up and top-down methods and used to create the S4 deposition velocity map, are maximum at the end of August or the beginning of September. Moreover, the observed mixing ratios, which are dominated by the uptake in the HNH, are minimum at the end of summer as well. The shift from June to August shows that we are able to reproduce the seasonal cycle of the soil uptake better than with the previous assumptions. In the Tropics and the Southern Hemisphere, no seasonal cycle is apparent and the mean value is consistent among all of the scenarios.

In S0, it was believed that the soil sink was too weak in the HNH (Hauglustaine and Ehhalt, 2002), so in S1 and S2 we have increased this sink by 30%.

In S1, we still invert the net H_2 flux and the soil sink remains nearly the same as the prior flux. In S2, since we separately invert the soil sink and the surface emissions, the deposition velocities are optimised and the resulting HNH soil uptake is nearly back to the value of S0. This seems to imply that the soil uptake in S0 was not that weak but that the offset between the simulated mixing ratios and observations has other causes.

Overall, the seasonal cycle of the surface emissions peaks in the HNH in June for S0 to S2 and in August for S3 to S5. This can be explained by the change in the seasonality of the soil uptake which shifts from June to August as well, highlighting the fact that the different processes are not completely independently inverted. In the Tropics, two maxima are observed, one in March and the second in September. They coincide with the biomass burning maxima of each hemisphere, in March in the south

ACPD
10, 28963–29005, 2010

and in August/September in the north (van der Werf et al., 2006). Bousquet et al. (2010) found two peaks as well, the first one in mid-March and the second, which is also the larger one, in September. S2, S4 and S5 reproduce this same pattern. The southern maximum is clearly apparent for S1, S2 and S5 but weak for S0, S3 and S4. Except for S1, the second maximum in September is larger. We observe good agreement among all of the scenarios, except for S0, for the amplitude of the summer peak. In the Southern Hemisphere, there are only very small surface emissions.

In S5, we have separately inverted the emissions in three different processes. Biomass burning (dark green dots), anthropogenic (dark green dashes) and N_2 fixation-related (dark green dashes-dots) emissions are plotted in the same panel as the total surface emissions are. The prior is overplotted in light green with the same symbols for each source. The seasonality is mainly driven by the biomass burning emissions whereas the anthropogenic and N_2 fixation-related emissions are more or less constant throughout the year.

From the analysis of the differences between the observations and the simulated mixing ratios and from these last remarks, it can be concluded that S5 is the more pertinent scenario. Therefore, the following discussion on the H_2 budget focuses on the results of this scenario.

4.3 H_2 budget

In Table 4, the mean estimation for each term of the global and regional budget is calculated for 2007, 2008 and the whole period based on scenario S5. The global estimations for each term as given in Xiao et al. (2007) and Bousquet et al. (2010) are added in Table 4. The uncertainties for our study are represented by the standard deviation of scenarios S1 through S5. We do not include S0 because, in this scenario, the prior HCHO flux is $\approx 5\,\mathrm{Tg\,yr^{-1}}$ lower than the prior flux in the other scenarios and, as explained previously, prescribed with small uncertainties. Moreover, the uncertainties of Table 4 do not include all of the sources of uncertainties. They should therefore be considered as a lower estimate. For Bousquet et al. (2010), we have indicated the

ACPD
10, 28963–29005, 2010

standard deviation of the sensitivity inversions based on the reference scenario (external errors). The errors in Xiao et al. (2007) include model uncertainties, absolute calibration error and errors in the assumed transportation source strength. For each region, we indicate the relative proportion of each regional source or sink in comparison with the global source or sink. Figure 7 represents this budget per process and per region. All of the scenarios produce a consistent process-based view (maximum standard deviation of 15%). From a region-based view, the total H_2 flux ranges between −8 and +8 Tg yr^{-1}. For these small fluxes, it is not adequate to use the relative standard deviation (varying between 18% and 160%) but we observe standard deviations below 2 Tg yr^{-1}. For all of the scenarios, the HNH is a net sink of H_2 and the Tropics are a net source. Globally, ≈47 Tg yr^{-1} of H_2 are produced by photochemical production and ≈18 Tg yr^{-1} are consumed by the OH reaction. Approximately 36 Tg yr^{-1} are emitted and ≈59 Tg yr^{-1} are deposited in the soils. This budget leads to a tropospheric burden of 166 Tg and a life time of 2.2 years. This budget is consistent with most of the previous studies about H_2 cycle.

Every process has a larger flux in the Tropics than it has in the HNH or HSH. Tropical processes represent between 55% and 74% of global processes depending on the flux types. Indeed, the photochemical production and the OH sink depend strongly on insolation which is maximum in the Tropics. The tropical maximum in the surface emissions is due to biomass burning emissions. For the maximum of soil uptake in the Tropics (55%), as Xiao et al. (2007) have already proposed, one explanation could be that the tropical soils are more efficient in terms of uptake than the extra-tropical soils are. It could also be linked to the optimum conditions in the humidity and temperature of this region. The soil sink in the HNH nevertheless represents 40% of the global soil sink.

The mean values of the global budget remain, within the uncertainties, compatible with the one presented in Bousquet et al. (2010). The budget from Xiao et al. (2007) differs significantly except for the OH loss. Their emissions are lower but their photochemical production and their soil uptake are more than 20 Tg yr^{-1} larger than in our

ACPD
10, 28963–29005, 2010

work. The repartition between the different regions is more consistent with Xiao et al. (2007) than with Bousquet et al. (2010). This result can be explained by the fact that, in this study and in Xiao et al. (2007), the budget was analysed through the same latitudinal bands, whereas Bousquet et al. (2010) used large regions that did not exactly fit these latitudinal bands. Finally, our estimate of biomass burning-related emissions is the same order of magnitude as Bousquet et al. (2010) and Xiao et al. (2007) but our estimation represents only 22% of the total emissions against 31% and 44% for Bousquet et al. (2010) and Xiao et al. (2007), respectively.

4.4 Focus on Europe

In this study, Europe contains the largest number of observation sites. Therefore, one can expect to have sufficient constraints to improve our knowledge on the sources and sinks of H_2 for this part of the world. As seen in Fig. 7, Europe, as part of the HNH, seems to be a net sink of H_2. In Fig. 8, the posterior flux map and the difference between posterior and prior in percentage of the prior for the S5 surface emissions and soil uptake are plotted. To observe the difference better, the data are interpolated on a higher resolution grid ($1^\circ \times 1^\circ$). The emissions in Europe present the same pattern in the spring and autumn. However, in the autumn, the emissions are slightly higher (maximum of $8\,\mathrm{Tg\,yr^{-1}}$), than they are in the spring (maximum of $5\,\mathrm{Tg\,yr^{-1}}$). This autumnal flux can be explained, from the seasonal cycle (see Fig. 6), by a combination of enhanced biomass burning and N_2 fixation-related emissions at the end of the summer and a small increase of the anthropogenic emissions at the end of the year. The differences between prior and posterior range from −60 to 0% in spring and from −15 to +30% in autumn for the emissions. This means that in spring, the inversion reduces European prior emissions, especially in western Europe. In autumn, western prior emissions are only slightly decreased, but eastern prior emissions are largely increased by the inversion. Globally, the spring soil uptake is smaller than the autumn soil uptake especially in the boreal region and the south of Europe. The uptake in central Europe, smaller in autumn than in summer, may be explained by early snow in

ACPD
10, 28963–29005, 2010

the alpine region in autumn. The differences between prior and posterior range from −7 to +35% in spring and from −58 to +10% in autumn. The spring soil uptake is increased in all of Europe compared to the prior estimate. In autumn, a large decrease of the prior soil uptake is found for northern Europe, whereas western Europe flux is increased compared to the prior.

In Table 5, the emissions and the soil uptake are detailed for seven countries or groups of countries in Table 5: geographical Europe (including the European part of Russia, west of the Ural mountains); Europe (27 countries); France; Germany; the United Kingdom and Ireland; Scandinavia and Finland; Spain, Italy and Portugal. In terms of emissions, geographical Europe represents 6% and 18% of the global and HNH emissions respectively. The European soil uptake accounts for 7% and 17% of the global and HNH uptake respectively. Anthropogenic emissions account for 52% of the total emissions globally, 62% in the HNH and 72% in Europe (27 countries). In Europe, depending on the countries, anthropogenic emissions account for 50% to 100% of the total emissions. As written above, there is no bottom-up inventory of H_2 emissions. We have then compared our results with the inventory from the Institute for Energy and Environmental Research (IEER) (Thiruchittampalam and Köble, 2004), which is not used as prior information (see Table 5). We have scaled the CO emissions with the anthropogenic H_2/CO mass ratio of 0.034 as found in Yver et al. (2009). The two sets of values agree well with one another. The mean difference lies around 10%. Uncertainties on inventories are not yet produced quantitatively but the EDGAR database has proposed ranges of uncertainties: low (±10%), medium (±50%) and large (±100%) (Olivier et al., 1996). For CO, most uncertainties by source types are reported as “medium”, therefore making our results consistent with IEER estimates, within their respective uncertainties.

ACPD
10, 28963–29005, 2010

5 Conclusions

This work presents the results of an inversion of tropospheric H_2 sources and sinks at a grid cell resolution for the period between mid-2006 and mid-2009. The model focuses on soil uptake and surface emissions. Overall, the results of this study agree with those of previous studies with regard to a lifetime of about two years, a soil uptake of ≈58 Tg yr^{-1} and emissions of ≈34 Tg yr^{-1} for a total source of ≈80 Tg yr^{-1}. All of the inversions performed with the six scenarios are fairly consistent with one another in terms of the processes (standard deviation ≈15%) and the regions (standard deviation <2 Tg yr^{-1}). From the several scenarios that have been elaborated, the best one (S5) in terms of fit to the mean atmospheric mixing ratio, seasonal cycle and flux measurements combines a separate inversion of the soil sink and of the sources in three terms and a soil deposition velocity map based on soil uptake measurements. Our estimation for the global soil uptake is -59 ± 4 Tg yr^{-1}. Ninety-five per cent of this uptake is located in the HNH (40%) and the Tropics (55%). No significant trend is found for the soil uptake or any of the other processes of the H_2 budget throughout 2006–2009. To study the emissions better, one scenario (S5), has been implemented with a separate inversion of the sources in three processes (biomass burning, fossil fuel and N_2 fixation related emissions). This scenario shows that the seasonal variability of the emissions is mainly driven by the biomass burning emissions. Finally, we have focused our analysis on Europe and compared the anthropogenic emissions with a CO inventory scaled with a H_2/CO mass ratio of 0.034. Anthropogenic emissions represent 50% to 100% of the total emissions depending on the country. The model and the inventory agree with one another within their respective uncertainties. A further step will be to invert other relevant species with H_2 such as CH_4, CO and HCHO, which is a unique capability of our multispecies inversion system (Pison et al., 2009). In particular, the optimisation of the HCHO flux, which is fixed in this work, would have an important influence on the H_2 budget through the process of photochemical production.

ACPD
10, 28963–29005, 2010

Future inversions of H_2 sources and sinks should gain robustness by including observations of other networks but also by including observations of the deuterium enrichment of H_2 (δD of H_2), as shown in Rhee et al. (2006); Price et al. (2007). Several groups have produced δD observations (Gerst and Quay, 2001; Rahn et al., 2003; Röckmann et al., 2003; Rhee et al., 2006; Price et al., 2007). Within the EUROHYDROS project, δD observations from six sampling sites are available for the recent years (from 2006). The isotopic signatures for fossil fuel, biofuel, biomass burning, and ocean sources are all depleted in δD relative to the atmosphere, whereas photochemical production of H_2 has a large positive isotopic signature. On the sink side, OH loss fractionates more than soil uptake (Price et al., 2007). The tropospheric δD is about $+130 \pm 4\%$ (Gerst and Quay, 2000). Assimilating δD observations together with H_2 observations could bring new constraints on H_2 budget if the different isotopic signatures can be determined with a good precision.

Acknowledgements. We gratefully thank Mathilde Grand and Vincent Bazantay for performing the flasks and in-situ analyses for the RAMCES network as well as the people involved in the samplings and analyses for the EUROHYDROS network. Thank you to Frédéric Chevallier for the precious help on the modelling part and to the computing support team of the LSCE. This work was carried out under the auspices of the 6th EU framework program # FP6-2005-Global-4 "EUROHYDROS- A European Network for Atmospheric Hydrogen Observations and Studies". RAMCES is funded by INSU and CEA.

The publication of this article is financed by CNRS-INSU.

ACPD
10, 28963–29005, 2010

References

Aalto, T., Lallo, M., Hatakka, J., and Laurila, T.: Atmospheric hydrogen variations and traffic emissions at an urban site in Finland, Atmos. Chem. Phys., 9, 7387–7396, doi:10.5194/acp-9-7387-2009, 2009. 28970

Bonasoni, P., Calzolari, F., Colombo, T., Corazza, E., Santaguida, R., and Tesi, G.: Continuous CO and H_2 measurements at Mt. Cimone (Italy): Preliminary results, Atmos. Environ., 31, 959–967, 1997. 28970

Bond, S., Vollmer, M., Steinbacher, M., Henne, S., and Reimann, S.: Atmospheric molecular hydrogen (H_2): Observations at the high-altitude site Jungfraujoch, Switzerland, Tellus B, doi:10.1111/j.1600-0889.20100059.x, 2010. 28970

Bousquet, P., Hauglustaine, D. A., Peylin, P., Carouge, C., and Ciais, P.: Two decades of OH variability as inferred by an inversion of atmospheric transport and chemistry of methyl chloroform, Atmos. Chem. Phys., 5, 2635–2656, doi:10.5194/acp-5-2635-2005, 2005. 28973, 28974

Bousquet, P., Yver, C., Pison, I., Li, Y. S., Fortems, A., Hauglustaine, D., Szopa, S., Peylin, P., Novelli, P., Langenfelds, R., Steele, P., Ramonet, M., Schmidt, M., Simmonds, P. G., Foster, P., Morfopoulos, C., and Ciais, P.: A 3-D inversion of the global hydrogen cycle: implications for the soil uptake flux, J. Geophys. Res., accepted, 2010. 28968, 28976, 28981, 28982, 28983, 28996

Brasseur, G. P., Hauglustaine, D. A., Walters, S., Rasch, P. J., Müller, J., Granier, C., and Tie, X. X.: MOZART, a global chemical transport model for ozone and related chemical tracers 1. Model description, J. Geophys. Res., 103, 28265–28290, 1998. 28975

Carouge, C., Bousquet, P., Peylin, P., Rayner, P. J., and Ciais, P.: What can we learn from European continuous atmospheric CO_2 measurements to quantify regional fluxes – Part 1: Potential of the 2001 network, Atmos. Chem. Phys., 10, 3107–3117, doi:10.5194/acp-10-3107-2010, 2010. 28974

Chevallier, F., Fisher, M., Peylin, P., Serrar, S., Bousquet, P., Bréon, F., Chédin, A., and Ciais, P.: Inferring CO2 sources and sinks from satellite observations: Method and application to TOVS data, J. Geophys. Res., 110, D24309, doi:10.1029/2005JD006390, 2005. 28972, 28974

Conrad, R. and Seiler, W.: Decomposition of Atmospheric Hydrogen By Soil Microorganisms and Soil Enzymes, Soil Biol. Biochem., 13, 43–49, 1981. 28966

ACPD
10, 28963–29005, 2010

Conrad, R. and Seiler, W.: Influence of temperature, moisture, and organic carbon on the flux of H_2 and CO between soil and atmosphere: Field studies in subtropical regions, J. Geophys. Res., 90, 5699–5709, 1985. 28966

Ehhalt, F. R. D. H.: The tropospheric cycle of H_2: A critical review, Tellus B, 61, 500–535, 2009. 28966, 28967

Engel, A.: EUROHYDROS, A European Network for Atmospheric Hydrogen observations and studies., in: EUROHYDROS Final Report, http://cordis.europa.eu/fetch?CALLER=FP6_PROJ&ACTION=D&DOC=1&CAT=PROJ&QUERY=012bab525b95:d528:5b2afd2e&RCN=80080, 2009. 28967, 28970, 28971

Erickson, D. J. and Taylor, J. A.: 3-D tropospheric CO modeling - The possible influence of the ocean, Geophys. Res. Lett., 19, 1955–1958, 1992. 28975

Gerst, S. and Quay, P.: The deuterium content of atmospheric molecular hydrogen: Method and initial measurements, J. Geophys. Res., 105, 26433–26446, 2000. 28986

Gerst, S. and Quay, P.: Deuterium component of the global molecular hydrogen cycle, J. Geophys. Res., 106, 5021–5029, 2001. 28986

Granier, C., Hao, W. M., Brasseur, G., and Müller, J.-F.: Land use practices and biomass burning: Impact on the chemical composition of the atmosphere, in Biomass Burning and Global Change, edited by: Levine, J. S., MIT Press, Cambridge, Mass., 1996. 28975

Grant, A., Witham, C. S., Simmonds, P. G., Manning, A. J., and O'Doherty, S.: A 15 year record of high-frequency, in situ measurements of hydrogen at Mace Head, Ireland, Atmos. Chem. Phys., 10, 1203–1214, doi:10.5194/acp-10-1203-2010, 2010b. 28966, 28970

Hammer, S. and Levin, I.: Seasonal variation of the molecular hydrogen uptake by soils inferred from continuous atmospheric observations in Heidelberg, southwest Germany, Tellus, 61B, 556–565, 2009. 28969, 28970

Hammer, S., Vogel, F., Kaul, M., and Levin, I.: The H_2/CO ratio of emissions from combustion sources: comparison of top-down with bottom-up measurements in southwest Germany, Tellus, 61B, 547–555, 2009. 28970

Hao, W. M., Ward, D. E., Olbu, G., and Baker, S. P.: Emissions of CO_2, CO, and hydrocarbons from fires in diverse African savanna ecosystems, J. Geophys. Res., 101, 23577–23584, 1996. 28975

Hauglustaine, D. A. and Ehhalt, D. H.: A three-dimensional model of molecular hydrogen in the troposphere, J. Geophys. Res., 107, 4330, doi:10.1029/2001JD00156, 2002. 28966, 28967, 28973, 28974, 28975, 28976, 28980, 29001

Hauglustaine, D. A., Hourdin, F., Jourdain, L., Filiberti, M. A., Walters, S., Lamarque, J. F., and Holland, E. A.: Interactive chemistry in the Laboratoire de Meteorologie Dynamique general circulation model: Description and background tropospheric chemistry evaluation, J. Geophys. Res., 109, D04314, doi/10.1029/2003JD003957, 2004. 28973

Hough, A. M.: Development of a Two-Dimensional Global Tropospheric Model: Model Chemistry, J. Geophys. Res., 96, 7325–7362, 1991. 28975

Hourdin, F. and Armengaud, A.: The Use of Finite-Volume Methods for Atmospheric Advection of Trace Species. Part I: Test of Various Formulations in a General Circulation Model, Mon. Weather Rev., 127, 822–837, 1999. 28972

Hourdin, F. and Talagrand, O.: Eulerian backtracking of atmospheric tracers. I: Adjoint derivation and parametrization of subgrid-scale transport, Q. J. Roy. Meteorol. Soc., 132, 567–583, 2006. 28972

Jordan, A.: The EUROHYDROS calibration scale for hydrogen, 14th WMO/IAEA Meeting of Experts on Carbon Dioxide, Other Greenhouse Gases, and Related Tracer Measurement Techniques, 2007. 28970

Jordan, A. and Steinberg, B.: Calibration of atmospheric hydrogen measurements, Atmos. Meas. Tech. Discuss., 3, 4931–4966, doi:10.5194/amtd-3-4931-2010, 2010. 28970

Khalil, M. A. K. and Rasmussen, R. A.: Global increase of atmospheric molecular hydrogen, Nature, 347, 743–745, 1990. 28966

Krol, M. C., Lelieveld, J., Oram, D. E., Sturrock, G. A., Penkett, S. A., Brenninkmeijer, C. A. M., Gros, V., Williams, J., and Scheeren, H. A.: Continuing emissions of methyl chloroform from Europe, Nature, 421, 131–135, 2003. 28973, 28974

Lallo, M., Aalto, T., Laurila, T., and Hatakka, J.: Seasonal variations in hydrogen deposition to boreal forest soil in southern Finland, Geophys. Res. Lett., 35, L04402, doi:10.1029/2007GL032357, 2008. 28966, 28969

Lallo, M., Aalto, T., Hatakka, J., and Laurila, T.: Hydrogen soil deposition at an urban site in Finland, Atmos. Chem. Phys., 9, 8559–8571, doi:10.5194/acp-9-8559-2009, 2009. 28966, 28969

Lamarque, J.-F., Granier, C., Bond, T., Eyring, V., Heil, A., Kainuma, M., Lee, D., Liousse, C., Mieville, A., Riahi, K., Schultz, M., Smith, S., Stehfest, E., Stevenson, D., Thomson, A., Aardenne, J. V., and Vuuren, D. V.: Gridded emissions in support of IPCC AR5, IPCC, 34, 2008. 28975, 28976

Langenfelds, R. L., Francey, R. J., Pak, B. C., Steele, L. P., Lloyd, J., Trudinger, C. M., and

ACPD
10, 28963–29005, 2010

Allison, C. E.: Interannual growth rate variations of atmospheric CO 2 and its delta 13 C, H 2, CH 4, and CO between 1992 and 1999 linked to biomass burning, Global Biogeochem. Cy., 16, 1048, doi:10.1029/2001GB001466, 2002. 28967

Müller, J.: Geographical Distribution and Seasonal Variation of Surface Emissions and Deposition Velocities of Atmospheric Trace Gases, J. Geophys. Res., 97, 3787–3804, 1992. 28975

Novelli, P. C., Lang, P. M., Masarie, K. A., Hurst, D. F., Myers, R., and Elkins, J. W.: Molecular hydrogen in the troposphere – Global distribution and budget, J. Geophys. Res., 104, 30427–30444, 1999. 28965, 28966, 28967

Olivier, J. G. J., Bouwman, A. F., van der Maas, C. W. M., Berdowski, J. J. M., Veldt, C., Bloos, J. P. J., Visschedijk, A. J. H., Zandveld, P. Y. J., and Haverlag, J. L.: Description of EDGAR Version 2.0: A set of global emission inventories of greenhouse gases and ozone-depleting substances for all anthropogenic and most natural sources on a per country basis and on 1 degree x 1 degree grid, Rijksinstituut voor Volksgezondheid en Milieu RIVM, 1996. 28975, 28984

Pison, I., Bousquet, P., Chevallier, F., Szopa, S., and Hauglustaine, D.: Multi-species inversion of CH_4, CO and H_2 emissions from surface measurements, Atmos. Chem. Phys., 9, 5281–5297, doi:10.5194/acp-9-5281-2009, 2009. 28972, 28973, 28975, 28985, 28995

Price, H., Jaegle, L., Rice, A., Quay, P., Novelli, P. C., and Gammon, R.: Global budget of molecular hydrogen and its deuterium content: Constraints from ground station, cruise, and aircraft observations, J. Geophys. Res., 112, 22108, doi:10.1029/2006JD008152, 2007. 28966, 28967, 28986

Prinn, R. G., Weiss, R. F., Fraser, P. J., Simmonds, P. G., Cunnold, D. M., Alyea, F. N., O'Doherty, S., Salameh, P., Miller, B. R., Huang, J., Wang, R. H. J., Hartley, D. E., Harth, C., Steele, L. P., Sturrock, G., Midgley, P. M., and McCulloch, A.: A history of chemically and radiatively important gases in air deduced from ALE/GAGE/AGAGE, J. Geophys. Res., 105, 751–792, 2000. 28967

Prinn, R. G., Huang, J., Weiss, R. F., Cunnold, D. M., Fraser, P. J., Simmonds, P. G., McCulloch, A., Harth, C., Reimann, S., and Salameh, P.: Evidence for variability of atmospheric hydroxyl radicals over the past quarter century, Geophys. Res. Lett., 32, L07809, doi:10.1029/2004GL022228, 2005. 28973, 28974

Rahn, T., Eiler, J. M., Boering, K. A., Wennberg, P. O., McCarthy, M. C., Tyler, S., Schauffler, S., Donnelly, S., and Atlas, E.: Extreme deuterium enrichment in stratospheric hydrogen and the global atmospheric budget of H_2, Nature, 424, 918–921, 2003. 28986

ACPD
10, 28963–29005, 2010

Rhee, T. S., Brenninkmeijer, C. A. M., and Röckmann, T.: The overwhelming role of soils in the global atmospheric hydrogen cycle, Atmos. Chem. Phys., 6, 1611–1625, doi:10.5194/acp-6-1611-2006, 2006. 28986
Röckmann, T., Rhee, T. S., and Engel, A.: Heavy hydrogen in the stratosphere, Atmos. Chem. Phys., 3, 2015–2023, doi:10.5194/acp-3-2015-2003, 2003. 28986
Sadourny, R. and Laval, K.: January and July performance of the LMD general circulation model, New Perspectives in Climate Modelling, 16, 173–197, 1984. 28972
Sanderson, M. G., Collins, W. J., Derwent, R. G., and Johnson, C. E.: Simulation of Global Hydrogen Levels Using a Lagrangian Three-Dimensional Model, J. Atmos. Chem., 46, 15–28, 2003. 28966
Schillert, A.: Parameters influencing the seasonality of H2 uptake in soils, State Examination Thesis, 2010. 28970, 28976, 29001
Schmidt, U.: The latitudinal and vertical distribution of molecular hydrogen in the troposphere, J. Geophys. Res., 83, 941–946, 1978. 28966
Schmitt, S., Hanselmann, A., Wollschläger, U., Hammer, S., and Levin, I.: Investigation of parameters controlling the soil sink of atmospheric molecular hydrogen, Tellus B, 61, 416–423, 2009. 28966, 28969
Sitch, S., Smith, B., Prentice, I. C., Arneth, A., Bondeau, A., Cramer, W., Kaplan, J. O., Levis, S., Lucht, W., Sykes, M. T., Thonicke, K., and Venevsky, S.: Evaluation of ecosystem dynamics, plant geography and terrestrial carbon cycling in the LPJ dynamic global vegetation model, Glob. Change Biol., 9, 161–185, 2003. 28976, 29001
Thiruchittampalam, B. and Köble, R.: European emissions map, Institute of Energy, Economics and the Rational Use of Energy (IER);University of Stuttgart, available at: http://carboeurope.ier.uni-stuttgart.de/, 2004. 28984, 28997
van der Werf, G. R., Randerson, J. T., Giglio, L., Collatz, G. J., Kasibhatla, P. S., and Arellano Jr., A. F.: Interannual variability in global biomass burning emissions from 1997 to 2004, Atmos. Chem. Phys., 6, 3423–3441, doi:10.5194/acp-6-3423-2006, 2006. 28981
Xiao, X., Prinn, R., Simmonds, P., Steele, L., Novelli, P., Huang, J., Langenfelds, R., O'Doherty, S., Krummel, P., and Fraser, P.: Optimal estimation of the soil uptake rate of molecular hydrogen from the Advanced Global Atmospheric Gases Experiment and other measurements, J. Geophys. Res., 112, DO7303, doi:10.1029/2006JD007241, 2007. 28966, 28967, 28981, 28982, 28983, 28996
Yonemura, S., Kawashima, S., and Tsuruta, H.: Continuous measurements of CO and H2

ACPD
10, 28963–29005, 2010

deposition velocities onto an andisol: uptake control by soil moisture, Tellus B, 51, 688–700, 1999. 28966

Yonemura, S., Kawashima, S., and Tsuruta, H.: Carbon monoxide, hydrogen, and methane uptake by soils in a temperate arable field and a forest, J. Geophys. Res., 105, 14347–14362, 2000a. 28966

Yonemura, S., Yokozawa, M., Kawashima, S., and Tsuruta, H.: Model Analysis of the Influence of Gas Diffusivity in Soil on Co and H2 Uptake, Tellus B, 52, 919–933, 2000b. 28966

Yver, C., Schmidt, M., Bousquet, P., Zahorowski, W., and Ramonet, M.: Estimation of the molecular hydrogen soil uptake and traffic emissions at a suburban site near Paris through hydrogen, carbon monoxide, and radon-222 semicontinuous measurements, J. Geophys. Res.-Atmos., 114, D18304, doi:10.1029/2009JD012122, 2009. 28970, 28976, 28984

ACPD

10, 28963–29005, 2010

Table 1. Flask sampling network sites (* RAMCES network (LSCE) sites additional to EUROHYDROS network).
LSCE: Laboratoire des Sciences du Climat et de l'Environnement, France; MPI-BGC : Max Planck Insitut für BiogGeoChemie, Germany; RHUL: Royal Holloway, University of London, UK; UHEI-IUP: Universität Heidelberg, Institut für Umweltphysik, Germany.

Code	Site	Latitude (°)	Longitude (°)	Altitude (m)	Beginning of H_2 analysis (mm/yy)	Isotopes	Laboratories
ALT	Alert	82.45	−62.52	210	05/07	no	LSCE
ALT	Alert	82.27	−62.31	177	10/04	no	MPI-BGC
ALT	Alert	82.45	−62.52	210	10/04	no	UHEI-IUP
AMS	Amsterdam Island	−37.95	77.53	150	01/05	yes	LSCE
BGU	Begur	41.97	03.3	30	09/05	no	LSCE
BIA	Bialystok	53.14	23.01	182	01/05	no	MPI-BGC
CGO*	Cape Grim	−40.68	144.68	94	03/06	no	LSCE
CPT	Cape Point	−34.35	18.48	260	03/05	no	LSCE
CVR	Cabo Verde	16.52	−24.52	18	03/07	yes	MPI-BGC
FIK	Finokalia	35.34	25.67	152	07/06	no	LSCE
GRI*	Griffin	56.62	−03.78	800–2000	02/06	no	LSCE
HLE	Hanle	32.78	78.96	4301	05/05	no	LSCE
HNG*	Hegyhatsal	46.95	16.65	344	07/05	no	LSCE
IVI*	Ivittuut	61.20	−48.18	15	09/07	no	LSCE
LPO	Ile Grande	48.80	−03.57	30	02/06	no	LSCE
MHD	Mace Head	53.33	−9.90	25	01/06	yes	LSCE
NMY	Neumayer	−70.65	−8.25	42	02/04	yes	UHEI
OXK	Ochsenkopf	53.14	23.01	1022	05/05	no	MPI-BGC
ORL*	Orleans	47.8	02.5	100–3000	06/05	no	LSCE
PDM	Pic du Midi	42.93	0.13	2877	09/05	no	LSCE
PON*	Pondichery	12.01	79.86	30	09/06	no	LSCE
PUY	Puy de Dôme	45.77	02.97	1465	03/06	no	LSCE
SCH	Schauinsland	47.92	7.92	1205	03/05	yes	UHEI-IUP
SIS	Shetland Island	60.05	−1.15	30	10/03	no	MPI-BGC
TRO	Troodos	35.07	−32.88	362	03/07	no	RHUL
TR3*	Trainou	47.96	02.11	311	08/06	no	LSCE
TVR*	Tver	82.45	−62.52	500–3000	08/04	no	LSCE
ZOT	Zotino	60.48	89.21	114	06/01	no	MPI-BGC

ACPD
10, 28963–29005, 2010

Table 2. EUROHYDROS continuous stations.
AGH-UST: University of Science and technology, Poland; EMPA: Swiss Federal Laboratories for Materials Science and Technology, Switzerland FMI: Finnish Meteorological Institute, Finland; LSCE: Laboratoire des Sciences du Climat et de l'Environnement, France; MGO:Main Geophysical Observatory, Russia; NILU : Norsk institutt for Luftforskning,Norway; RHUL: Royal Holloway, University of London, UK; UEA, University of East Anglia, UK; UFRA: University of Frankfurt, Institüt für Atmosphäre und Umwelt, Germany; UHEI-IUP: Universität Heidelberg, Institut für Umweltphysik, Germany; UNIURB: University of Urbino, Italy; UOB: University of Bristol, UK.

Code	Site	Latitude (°)	Longitude (°)	Altitude (m)	Beginning of H_2 analysis (mm/yy)	Laboratories
EGH	Egham	51.42	00.55	41	01/07	RHUL
GIF	Gif sur Yvette	48.70	02.01	20	06/06	LSCE
HEI	Heidelberg	49.40	08.70	116	01/05	UHEI-IUP
HEL	Helsinki	60.20	24.96	50	06/07	FMI
JUN	Jungfraujoch	46.55	7.98	3580	08/05	EMPA
KRK	Krakow	50.02	19.92	220	01/06	AGH-UST
MHD	Mace Head	53.33	−9.90	25	01/06	UOB
MTC	Monte Cimone	44.17	10.68	2165	08/07	UNIURB
PAL	Pallas	66.97	24.12	565	09/06	FMI
TNS	Taunus observatory	50.22	8.45	825	10/06	UFRA
VKV	Voiekovo	59.95	30.7	72	08/07	MGO
WAO	Weybourne	52.95	1.12	31	03/08	UEA
ZEP	Zeppelin	78.90	11.88	474	01/06	NILU

ACPD
10, 28963–29005, 2010

Table 3. Scenarios used in this study.

Scenario	Model	Prior
S0	original settings (H_2 net flux inverted)	original settings (as in Pison et al. (2009)
S1	original settings	new fluxes and new initial mixing ratios
S2	separate sink	new fluxes and new initial mixing ratios
S3	separate sink with LPJ deposition velocity map	new fluxes and new initial mixing ratios
S4	separate sink with Oslo CTM deposition velocity map	new fluxes and new initial mixing ratios
S5	separate sink and sources (biomass burning, fossil fuel and others) with Oslo deposition velocity map	new fluxes and new initial mixing ratios

ACPD
10, 28963–29005, 2010

Table 4. H_2 budget per process in Tg yr^{-1} (* in Bousquet et al. (2010) the fossil fuel and N_2 fixation related emissions are inverted together). The indicated error represents the standard deviation of the different scenarios for this study, the standard deviation of the sensitivity inversions for Bousquet et al. (2010) and for Xiao et al. (2007), the model uncertainties, absolute calibration error and errors in the assumed transportation source strength. The % represent the part of each regional term in the global term. The separated emission terms are not associated with error in this study as we did not perform several sensitivity tests.

Global	2007	2008		mid 2006-mid 2009	
			This study	Bousquet et al. (2010)	Xiao et al. (2007)
Biomass Burning	7.8	7.7	7.8	10±2	12±3
Fossil fuel	18.8	18.3	18.5	22±3*	15±10
N_2 fixation	9.5	9.4	9.4	*	–
Emissions	36.0±2.2	35.4±2.3	35.7±1.9	32±5	27±9
Photochemical production	46.9±0.1	46.5±0.1	46.5±0.1	48±4	76±13
OH loss	−18.1±1.0	−18.2±1.0	−18.2±1.0	−18±1	−18±3
Soil uptake	−58.0±4.2	−59.9±3.6	−58.8±4.0	−62±3	−84±8
North Hemisphere	2007	2008		mid 2006-mid 2009	
Biomass Burning	1.3	1.3	1.3		
Fossil fuel	8.3	8.0	8.0		
N_2 fixation	3.7	3.7	3.7		
Emissions	13.3±0.7	13.0±1.0	13.0±0.7 (36%)	50%	37%
Photochemical production	10.7±0.0	10.6±0.0	10.6±0.0 (23%)	33%	17%
OH loss	−2.9±0.1	−2.9±0.1	−2.9±0.1 (16%)	22%	12%
Soil uptake	−22.5±2.9	−23.8±2.2	−23.3±2.6 (40%)	53%	39%
Tropics	2007	2008		mid 2006-mid 2009	
Biomass Burning	6.3	6.3	6.4		
Fossil fuel	10.2	10.0	10.1		
N_2 fixation	5.1	5.1	5.1		
Emissions	21.6±1.6	21.3±1.4	21.6±1.2 (61%)	47%	62%
Photochemical production	32.2±0.0	31.9±0.0	31.9±0.0 (69%)	38%	75%
OH loss	−13.4±0.8	−13.4±0.8	−13.4±0.8 (74%)	50%	77%
Soil uptake	−32.5±2.1	−33.0±2.1	−32.6±2.1 (55%)	18%	55%
South Hemisphere	2007	2008		mid 2006-mid 2009	
Biomass Burning	0.1	0.1	0.1		
Fossil fuel	0.4	0.4	0.4		
N_2 fixation	0.6	0.6	0.6		
Emissions	1.1±0.0	1.1±0.0	1.1±0.0 (3%)	3%	1%
Photochemical production	4.1±0.0	4.0±0.0	4.0±0.0 (8%)	29%	8%
OH loss	−1.9±0.1	−1.9±0.1	−1.9±0.1 (10%)	28%	11%
Soil uptake	−3.0±0.4	−3.0±0.4	−3.0±0.4 (5%)	29%	6%

ACPD
10, 28963–29005, 2010

Table 5. H_2 budget per country in Europe in Tg yr^{-1}. In bold, the anthropogenic emissions from S5. In italics, the anthropogenic emissions from IEER (Thiruchittampalam and Köble, 2004).

Emissions (Tg yr^{-1})	2007	2008	mid 2006-mid 2009		
			Total	Anthropogenic	Anthropogenic from IEER
Europe (geographical)	2.2±0.1	2.3±0.3	2.2±0.5	**1.4**	*1.5*
Europe (27)	1.2±0.1	1.4±0.1	1.3±0.3	**0.9**	*1.0*
France	0.2 <0.1	0.2 <0.1	0.2±0.1	**0.2**	*0.2*
Germany	0.2 <0.1	0.2 <0.1	0.2±0.1	**0.1**	*0.1*
UK + Ireland	0.1 <0.1	0.1 <0.1	0.1 <0.1	**0.1**	*0.1*
Scandinavia + Finland	0.1 <0.1	0.1 <0.1	0.1 <0.1	**0.1**	*0.1*
Spain+Italy+Portugal	0.3 <0.1	0.3 <0.1	0.3 <0.1	**0.2**	*0.2*

Soil uptake (Tg yr^{-1})	2007	2008	mid 2006-mid 2009
Europe (geographical)	−3.9±0.9	−4.0±0.9	−3.9±1.1
Europe (27)	−1.6±0.5	−1.7±0.46	−1.6±0.6
France	−0.3 <0.1	−0.3 <0.1	−0.3±0.1
Germany	−0.2 <0.1	−0.2 <0.1	−0.2±0.1
UK + Ireland	−0.1 <0.1	0.0 <0.1	−0.1 <0.1
Scandinavia + Finland	−0.3±0.2	−0.4±0.2	−0.3±0.2
Spain+Italy+Portugal	−0.3±0.1	−0.3±0.1	−0.3±0.2

ACPD
10, 28963–29005, 2010

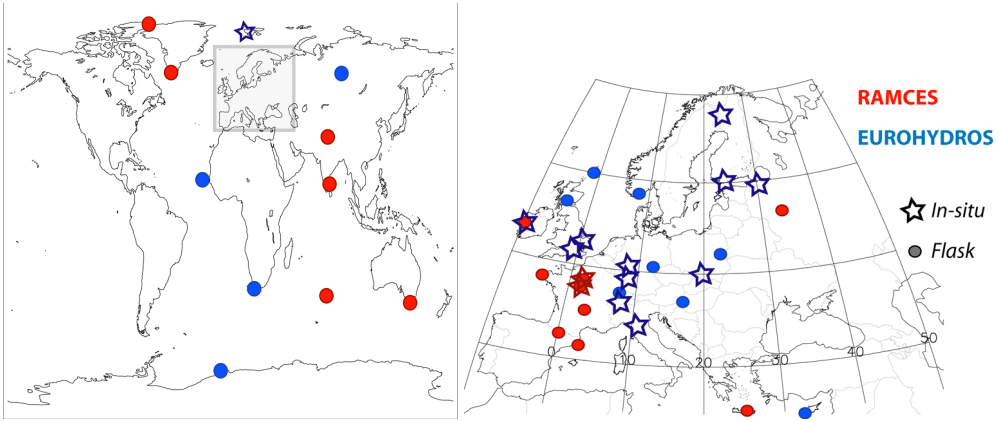

Fig. 1. EUROHYDROS and RAMCES sampling sites used in this study.

ACPD
10, 28963–29005, 2010

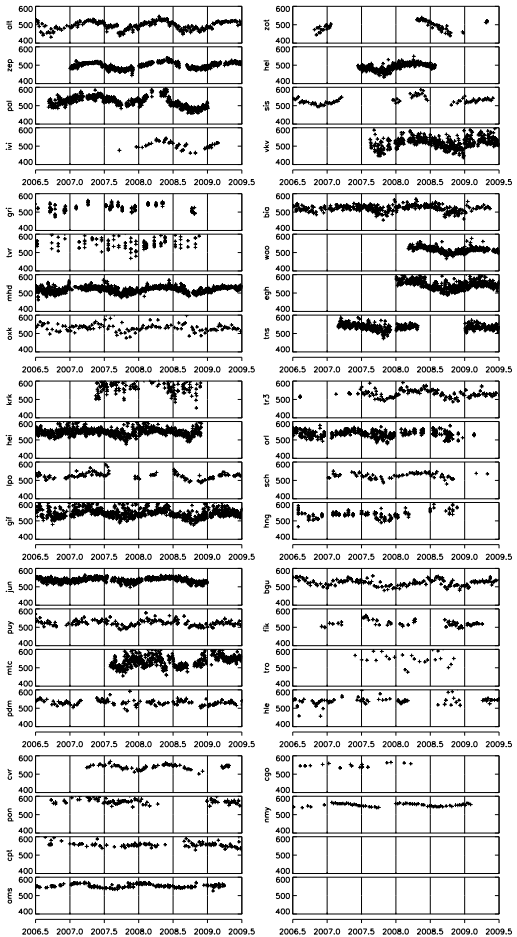

Fig. 2. H_2 time series for sampling sites from RAMCES and EUROHYDROS networks. Measurements are performed by 13 different European laboratories (see Table 1 and Table 2).

ACPD
10, 28963–29005, 2010

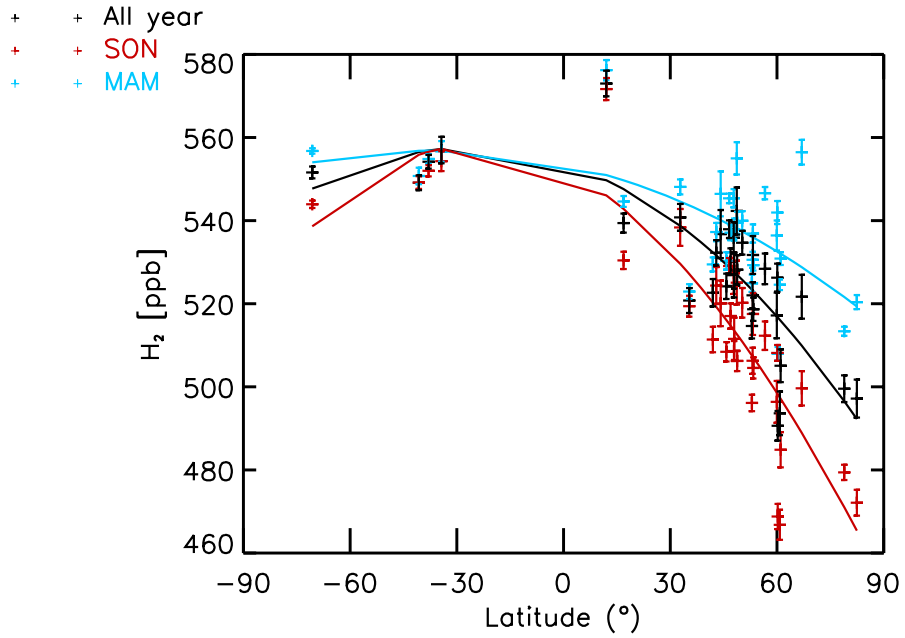

Fig. 3. H_2 mean mixing ratio latitudinal gradient. In black, for the whole year, in blue, for March, April, May (MAM) and in red for September, October and November (SON).

ACPD
10, 28963–29005, 2010

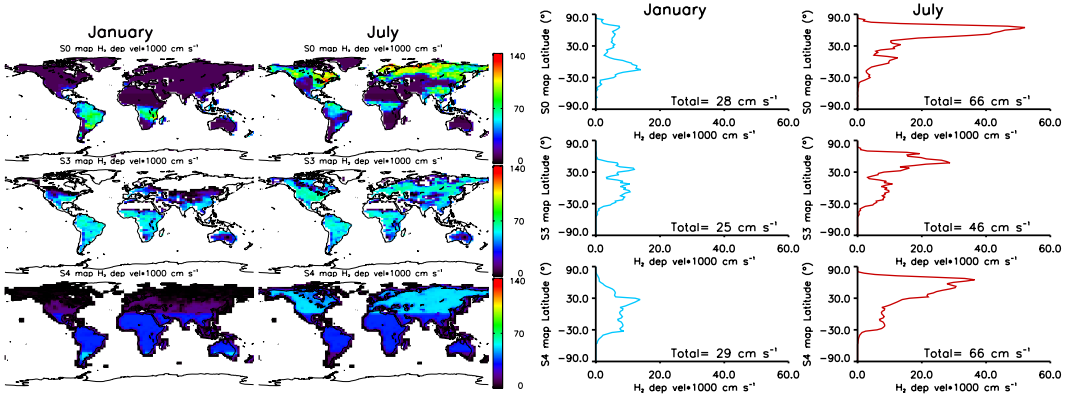

Fig. 4. On the left panel: the three soil deposition velocity maps used in this study. Right panel: the mean latitudinal deposition velocity is plotted against the latitude for each map. In each panel, top: from Hauglustaine and Ehhalt (2002), middle: from Sitch et al. (2003), bottom: from Schillert (2010) and Søvde.

ACPD
10, 28963–29005, 2010

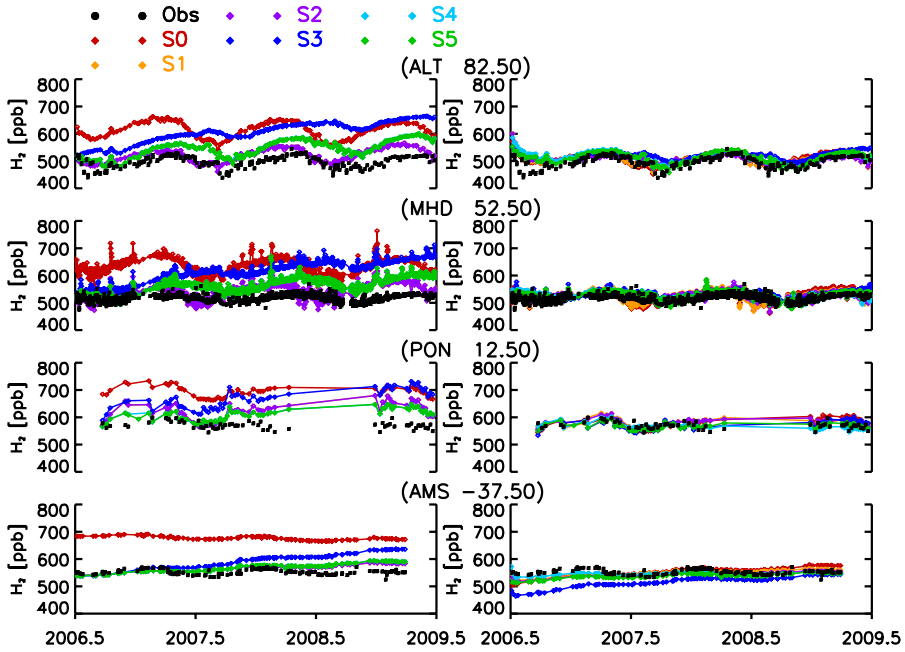

Fig. 5. H_2 mixing ratios at Alert, Mace Head, Pondichery and Amsterdam Island. Black filled circles plot the observations, diamonds simulated mixing ratios. Each scenario is represented by a different color, S0 and S1 in a red color scale, S2 to S4 in a blue color scale and S5 in green. On the left panel, the prior simulations and on the right panel, the posterior simulations.

ACPD
10, 28963–29005, 2010

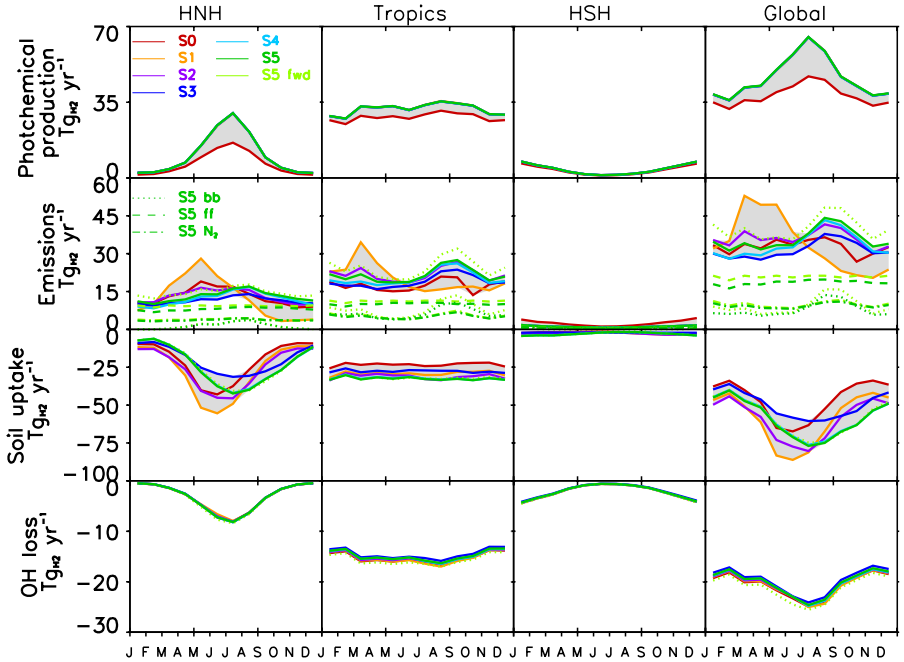

Fig. 6. Posterior seasonal cycle of H_2 fluxes for four regions (HNH: High North Hemisphere, above 30° N; Tropics, between 30° N and 30° S; HSH: High Southern Hemisphere, below 30° S). Each scenario is represented by a different color, S0 and S1 in red scale, S2 to S4 in blue scale and S5 in green. Separated emissions of S5 are plotted with dots for the biomass burning emissions, with dashes for the anthropogenic emissions and with dashes-dots for the N_2 fixation-related emissions.

ACPD
10, 28963–29005, 2010

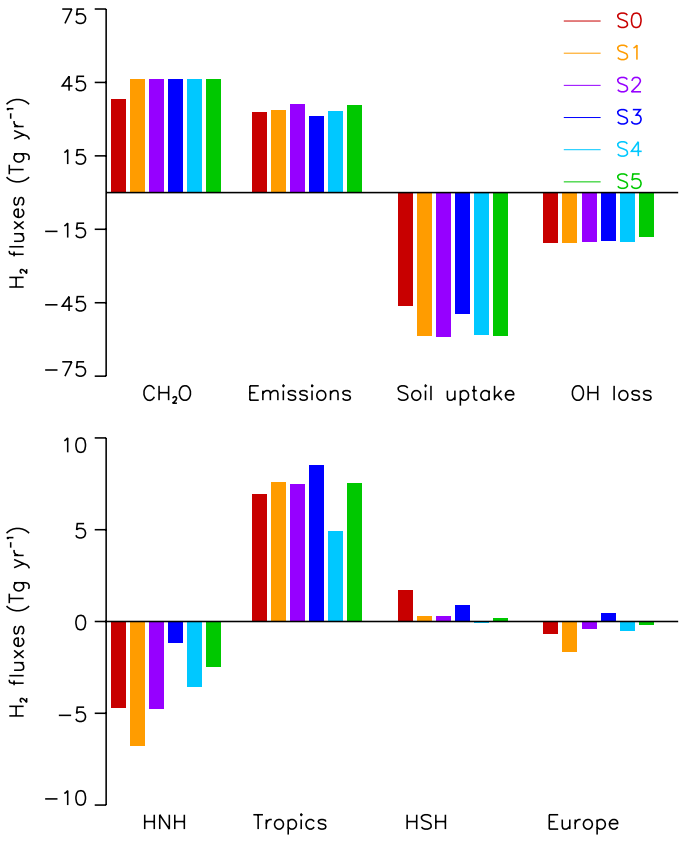

Fig. 7. Posterior H_2 budget per process (above) and regions (below). Each colour bar represents a scenario.

ACPD
10, 28963–29005, 2010

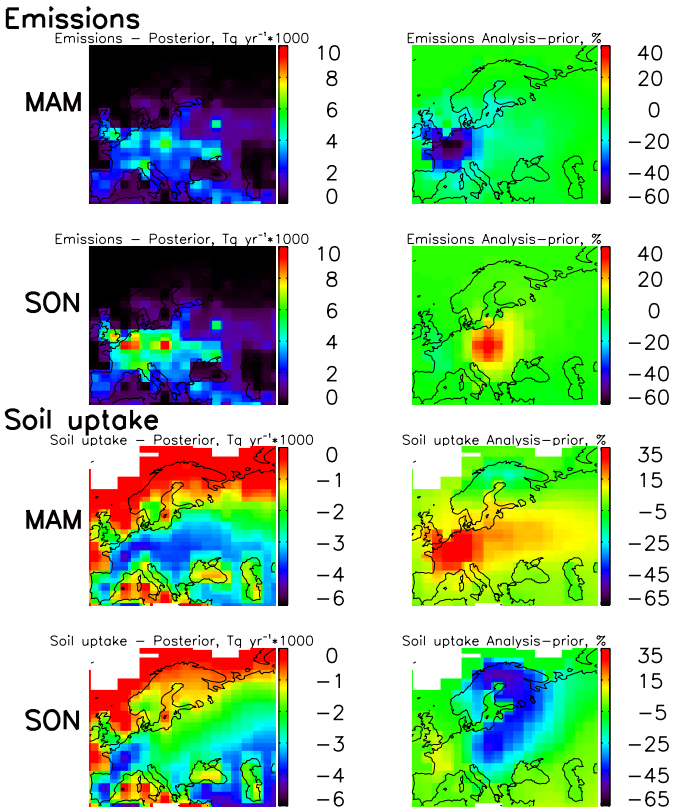

Fig. 8. S5 posterior flux map (on the left) and difference between S5 posterior and prior in % of the prior (on the right) fluxes for the surface emissions (above) and soil uptake (below) zoomed on Europe for March, April and May (MAM) and September, October and November (SON).

ACPD
10, 28963–29005, 2010